Phase-field modeling of constrained interactive fungal networks

Article *in* Journal of the Mechanics and Physics of Solids · December 2020

DOI: 10.1016/j.jmps.2020.104160

4 authors, including:

Farshad Ghanbari
Pennsylvania State University
2 PUBLICATIONS **8** CITATIONS
SEE PROFILE

Christian Peco
Pennsylvania State University
18 PUBLICATIONS **565** CITATIONS
SEE PROFILE

The following manuscript is the author's preprint version. For the published version that includes 3D fungal network simulations, please refer to https://doi.org/10.1016/j.jmps.2020.104160.

Phase-field modeling of constrained interactive fungal networks

F. Ghanbari[1], F. Costanzo[1], D. Hughes[2], C. Peco[1*]

1 *Department of Engineering Science and Mechanics, Penn State, USA*

2 *Department of Entomology, Penn State, USA*

Abstract

Fungi develop structures that interact with their surroundings and evolve adaptively in the presence of geometrical constraints, finding optimal solutions for complex combinatorial problems. The pathogenic fungus Ophiocordyceps constitutes a perfect model for the study of constrained interactive networks. Modeling these networks is challenging due to the highly coupled physics involved and their interaction with moving boundaries. In this work, we develop a computational phase-field model to elucidate the mechanics of the emerging properties observed in fungal networks. We use a variational approach to derive the equations governing the evolution in time of the mycelium biomass and the nutrients in the medium. We present an extensive testing of our model, reproduce growing and decaying phenomena, and capture spatial and temporal scales. We explore the variables interplay mechanism that leads to different colony morphologies, and explain abrupt changes of patterns observed in the laboratory. We apply our model to simulate analogous processes to the evolution of Ophiocordyceps as it grows through confined geometry and depletes available resources, demonstrating the suitability of the formulation to study this class of biological networks.

Keywords: Growth mechanics, Fungal infection, Constrained interactive network, Mycelia simulation

1. Introduction and background

Fungi are eukaryotic organisms defined by the presence of chitin in their cell walls, a mobility based on growth, and a heterotrophic character. Yeasts, molds, and mushrooms are examples found in this heterogeneous kingdom. Fungi are the main decomposers in nature. In their pluricellular form, fungi interact with the surrounding medium by growing a mycelium. The mycelium consists of a network of branching, cellular threads called hyphae, through which the fungus absorbs nutrients from its environment. The development and properties of these networks have interesting implications for different fields in science and engineering. For example, human-designed networks struggle to be optimal as the amount of interactions and data to process increase. Complex combinatorial problems are not easily treated with classical top-down design strategies, where a whole vision of the problem is required prior to design. In seeking for

*Correspondence to: christian.peco@psu.edu

alternatives, some bottom-up strategies [1] are inspired by the surprising success of very simple organisms to accomplish some of aforementioned challenging tasks. Examples of such strategies are found among social insects that construct large building-type structures with sophisticated ventilation systems, as termites [2], or hexagonal breeding lattices that maximize the space while using an optimal amount of material, as bees [3]. Experiments have shown the potential of fungi as paradigm for biologically-inspired bottom-up approaches. For example, a type of fungus revealed a strategy for the redesign of the railway network of Tokyo that was comparable in efficiency to that originally put forward by engineers [4]. Fungi could be crucial in developing scalable designs for growing systems in science.

Among fungi, Ophiocordyceps Unilateralis exhibits a very particular type of network. Ophiocordyceps is an insect-pathogenic fungus that parasitizes the ant genus Camponotus. During the infection process, this fungus develops a structure (mycelium) that alters and manipulates the host behavior, hence the colloquial denomination of its host as *zombie ant*. The cycle encompasses various stages, starting with the spores of Ophiocordyceps attaching to the ant's cuticle while foraging. Once the ant is infected, it experiences a variety of abnormal behaviors [5, 6] due to the growth and expansion of the fungus within the ant's head [7] (Fig. 1(a)). The nature of

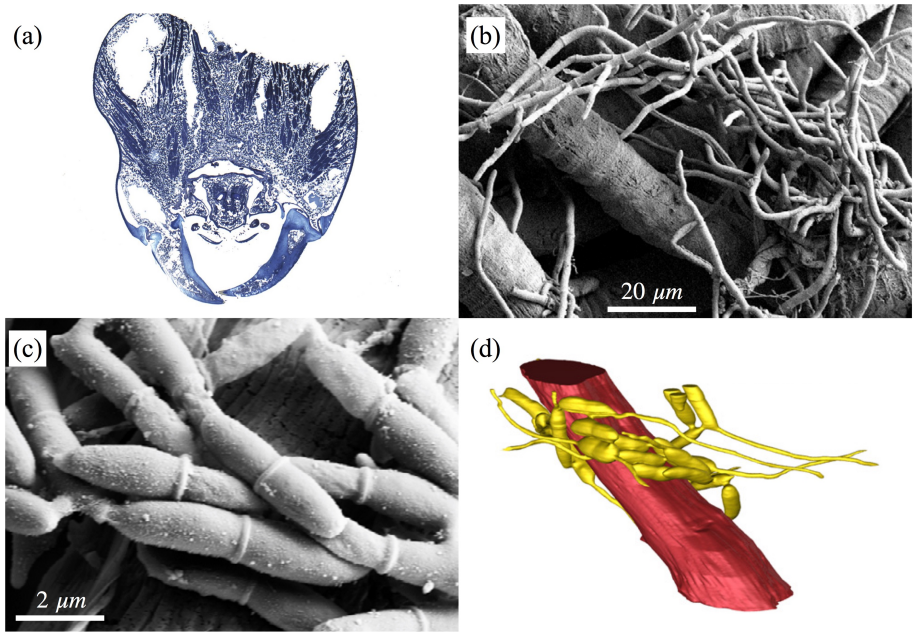

Figure 1. (a) Extensive fungal growth in the ant's head. (b) Aggregation of fungal cells in the infected muscle. (c) Magnification of the infected mandibular muscle. (d) Three-dimensional reconstructions of fungal network. A single fiber of an ant mandible (red) surrounded by hyphal bodies (yellow). Adapted from [7–9].

the fungal biomass can be observed at different scales in Fig. 1, where aggregates of individual hyphal threads (Fig. 1(c)) can be observed to form denser superstructures [8] (Fig. 1(b)). The fungus induced behaviors culminate with the ant climbing a plant and reaching a leaf holding proper conditions for (fungal) reproduction. The ant clings to the leaf by its mandibles and dies. Subsequently, a stalk (astroma) begins to grow from the back of the ant's head, ejecting

spores so that the fungus may infect more ants, closing the cycle [5]. Using electron microscopy, a 3-D reconstruction can be developed for the host and parasite tissue [9](Fig. 1(d)). The fungal network that takes control of the zombie ant presents some unique features, such as strong geometrical constraints and two-way interaction with the media. Not only do these traits make the infection interesting for entomologists, but they also represent an ideal example for the study of constrained interactive networks that is relevant to engineers.

In this paper, we present and explore a novel computational framework based on phase-fields to capture the physics of complex fungal networks, such as that built by Ophiocordyceps. We aim to elucidate the principles underpinning the growth behavior of fungi in general and Ophiocordyceps in particular. Our analysis will place special emphasis on growth in heterogeneous media with physical constraints and two-way interaction.

A review of fungal computational modeling and challenges

Modeling of fungal organisms presents difficulties due to the wide range of spatial and temporal scales involved, as well as the indeterminate nature of their growth habitats. Fungi exhibit processes that range from the sub-micron level to the tens of kilometers. They present metabolic reactions in the range of seconds, develop mycelial structures in the lapse of hours, and sustain their interaction with the media during hundreds of years. The complexity raises when the physical and nutritional heterogeneity of the host environment is taken into account [10]. Depending on this scale, fungus modeling is commonly categorized as microscale, intermediate or mesoscale, and macroscale. At the micro-scale level, the focus is set on modeling the hyphal tip growing mechanism. Best known micro-scale models include the steady-state model [11] and the vesicle supply center hypothesis [12, 13]. The steady-state model advocates for the continuous deposition of wall material at the hyphal tip and its subsequent fixation in the zone as the main extension mechanism. The second model revolves around the influence of a multicomponent pleomorphic structure found at hyphal apices. This structure is known as Spitzenkörper, and operates as a distribution point for vesicles carrying different cell wall materials and synthetic enzymes. Combinations of these two approaches have also been proposed [13, 14]. A more sophisticated vesicle supply mechanism for the Spitzenkörper was put forward in [15].

These micro-scale models provide a good intuition of the processes involved in the cellular tip extension, but do not explore the behavior and influence of the immediately surrounding network, which scale is considerably larger. This scale has been approached by the so-called intermediate scale models, which objective is to study the mycelium from the standpoint of absorption and redistribution of nutrients. Some of these models are discrete in nature, and describe individually the extension of hyphae using representative units. Some of these models have been very successful in reproducing particular growth network architectures [16–19]. Their network mechanics stem from internal nutrient concentrations and the transport of the wall building material vesicles reported in micro-scale studies, such as in [20–22]. The incorporation of the building material can be captured with a Michaelis-Mentis kinetic equation, establishing the rate at which new material is produced from a particular substrate. This abstraction can be informed from the micro-scale models. Nutrient transport inside the network is often modeled as a diffusive one, although other mechanisms seem to be involved in, for example, the movement of the vesicles thanks to the cytoskeleton [23]. Different types of nutrient and vesicles can be

considered in the pursue of more accurate descriptions of the extension process [22, 24]. An intermediate model focusing on nutrient and vesicle transport based on discrete units was put forward in [23]. The stochastic variability of fungal organisms was studied in [25] on a plant pathogenic fungi.

The main problem in using these discrete models to capture the response of global systems with variable conditions and high interactivity is that they do not rely on physical principles, but on statistical or heuristic rules that control the extension and branching phenomena. The limitations of discrete intermediate models with respect to the underlying development mechanics can be addressed with continuum intermediate modeling. These approaches aim to resolve the partial differential equations governing more global descriptions of the presence of the mycelium, such as cellular or hyphal density. Pioneering works in continuum modeling of fungi at the single colony level can be found in [26, 26, 27]. The first two works propose a one-dimensional formulation of extension and branching based on simple partial differential equations describing two variables, namely the number of filaments and number of tips in the system. The nutrient concentration is modeled as a diffusion process. The third work extends this idea to two and three dimensions, and focuses on branching and network architecture. These strategies were explored later by different authors. In [28], a model based on reaction-diffusion equations of a substrate and a biomass activator is presented, and then complemented in [29] by an additional variable giving more detail to nutrient transport. A similar idea is pursued in [17], in which an inhibitor variable is incorporated. A more sophisticated description of hyphal tips and an additional infectious equation was studied in [30]. The work in [31] was able to capture different network architectures using a hybrid model based on a two-dimensional cell lattice and a reaction-diffusion equation for the different components. Some of these ideas would be combined and extended in [32–34] for a macroscopic description of the mycelium, and in [35] to explore growth dynamics across a larger range of intermediate scales. Other models restrict to a particular growth aspect or environment feature, and hence propose a more sophisticated ordinary differential equation in to pursue of an accurate analysis of the target [36].

A phase-field continuum approach

Motivated by experimental observations in Ophiocordyceps, this paper focuses on setting the bases for a computational framework that is able to capture the evolution of fungal networks that evolve in strong geometrical and nutrient environments, and present complex two-way interactions with the media. Ophiocordyceps infection process within the ant's biomass poses several modeling questions regarding the influence of network geometry in the colonization and extraction of muscle fibers (Fig. 1), and the way rapidly changing nutrient conditions can affect the mycelium growth. The patterns described in different stages of the project suggest that a proper model should: (i) be based on mechanistic rules that can quantify the interplay of different agents and the fungal geometry, and (ii) should operate in the intermediate scale at a level of resolution that captures a first layer of geometrical abstraction, or basic network unit. The basic network unit can change between species. In the case of Ophiocordyceps, we refer to the aggregation of cells in branches with significant transport capacity. These observations seem to indicate an inadequacy of intermediate discrete approaches, due to their non-mechanistic approach and the possibility of having large number of cells in the system. Within the continuum

and hybrid models, as we have mentioned, we can find some modeling lines that present interesting features in the areas of nutrient internal transport and hyphal/tip behavior. However, these models tend to rely on reaction diffusion equations and hence the outcomes focus on the spreading of the biomass and its interaction with an environment of limited complexity. There is a gap when looking for formulations that combine the continuous description of intermediate scale physics with a continuous description of the biomass, and therefore able to capture architecture dynamics at the level shown by discrete strategies. In this paper, we propose a new approach based on phase-field modeling to overcome these obstacles.

Phase-field or diffuse interface models were originally formulated to describe vapor-liquid transitions by van der Walls [37], and by Cahn-Hilliard [38]. In the last decade, and aided by the increasing computational power, phase-field modeling has been extended and applied to a surprising variety of complex interface problems, such as anisotropic [39], thermal [40] and particulate fracture [41], or fluid biological membranes [42, 43]. Phase-field or diffuse interface methodologies avoid the tracking of moving fronts, replacing the otherwise implied boundary conditions by a partial differential equation that governs the evolution of a scalar field, defined over the whole domain. This is a critical advantage in the presence of highly dynamic geometries and/or variable topology. In addition, phase-field models are developed by recasting the physics of the system in terms of the new phase-field variable. Thus, the resulting evolution equations aim to describe the underlying mechanistic principles of the problem, instead of just using the phase-field variable as a marker, as is the case in traditional level-set methods. This particularity of phase-field models allows one to pose the problem from a variational form, beginning with a definition of the system's free energy. This free energy can be gradually expanded to introduce higher degrees of complexity in a straight-forward fashion. The potential of phase-field modeling, explored in different areas of science and engineering, has not gone unnoticed in other systems related to growth mechanics. Considerable work has been done in recent years in the field of tumor growth and tumor angiogenesis. A hybrid continuous-discrete approach in the pioneer work [44] presents a phase-field model to capture the evolution of the capillaries and angiogenic factors. In the spirit of this model, a high-order phase-field approach in [45] is proposed and resolved via isogeometric analysis. The model would be later refined in [46], and extended to three-dimensions in [47–49]. The model in [50] presents a phase-field model for carcinogenesis and solves the nonlinear partial differential equations (PDEs) using a finite element method and a stochastic collocation scheme. These studies demonstrate the potential of phase-field modeling for capturing the complexity of intermediate scale growth dynamics.

In this work, we present a continuum phase-field model to capture the mycelium evolution of fungi such as Ophiocordyceps at the intermediate scale. The remainder of the paper is organized as follows. In Section 2, we present the formulation of the fungal phase-field model in the continuum. The discretized model and numerical details are described in Section 3. Numerical results are presented in Section 4, devoted to perform an extensive testing of the method, and Section 5, where we show a variety of application results to illustrate the suitability of the formulation to study constrained interactive network development.

2. Continuum modeling of the fungal mycelium

2.1. Introduction

We develop the continuum formulation of a phase-field model that describes the evolution of a fungal mycelium embedded in a surrounding diffusive medium. The geometry of the system is defined by the open domain Ω and its boundary $\partial\Omega$, which reproduces the cuticle, considered impenetrable. The system is modeled with the variables ϕ and c, which quantify the presence of the biological solid and the nutrient concentration in the medium. The field ϕ is a phase-field variable taking values in the range $[0, 1]$, where 1 corresponds to the presence of fungal biomass and 0 represents its absence. This variable is a non-conserved order parameter that captures the evolution (growth, spreading, and death) of the fungal infection. Inclusions and other particularities of the ant's biomass can be represented by a secondary field η, which in this work is used to recreate geometrical constraints and different types of nutrient (such an organ containing a particular agent). The concentration of nutrients, symbolized by c, is modeled as a scalar field following a diffusive process. The incorporation of the hemolymph flow will be considered in a future publication. These concepts are sketched in Fig. 2.

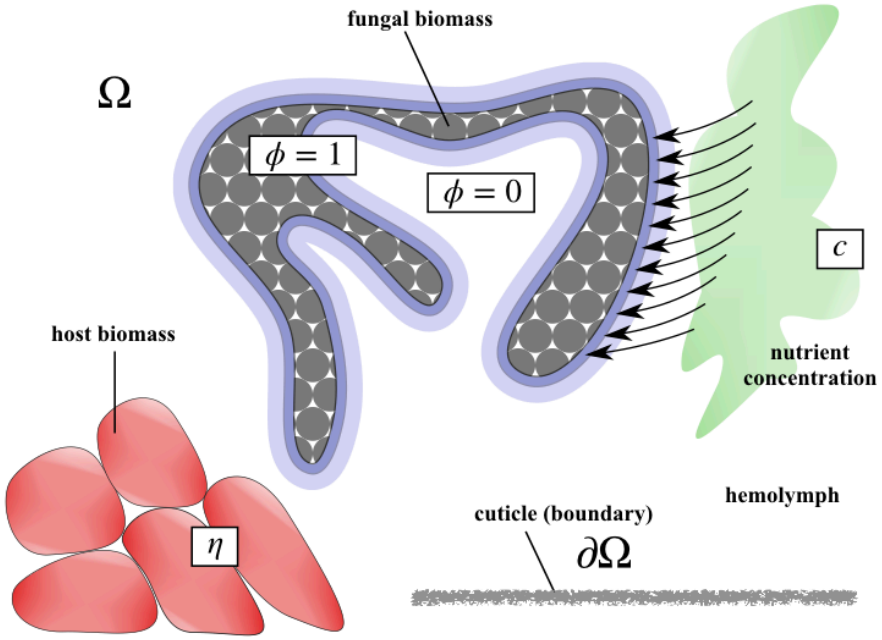

Figure 2. Sketch of the main components of the model. The domain Ω represents the body of the host. The phase-field variable ϕ indicates the portion of the domain occupied by the fungal organism. Nutrients contained by the hemolymph are represented by the concentration c. The geometry is set by the cuticle, considered rigid and unaffected by the fungus. Host biomass agents, such as muscle fiber contents, can be modeled with auxiliary variables (e.g., η).

2.2. Notation

We denote points in Ω by $\boldsymbol{x}$ and time by t. Given a vector or tensor field $\xi : \Omega \to \mathscr{V}$, where $\mathscr{V}$ stands for some appropriate vector space, the expressions $\nabla\xi$ and $\nabla \cdot \xi$ will denote the gradient and the divergence of ξ, respectively, where the spatial differentiation is carried out with respect to $\boldsymbol{x}$. For a vector or a tensor field ξ, the notation $|\xi|$ will denote the pointwise norm: $|\xi| = \sqrt{\xi \cdot \xi}$, the dot denoting an underlying inner product.

2.3. Free energy potential

We posit a fungal free energy potential Ψ with the following expression:

$$\Psi(\phi, \nabla\phi, c) = \int_\Omega F(\phi, \nabla\phi, c)\, dV_\Omega, \tag{1}$$

where the free energy density F is modeled as the sum of three contributions:

$$F(\phi, \nabla\phi, c) = I_\phi + W_\phi + B_\phi. \tag{2}$$

The first term on the right hand side I_ϕ, represents the interfacial energy, defined as

$$I_\phi = \tfrac{1}{2}\lambda^2 |\nabla\phi|^2, \tag{3}$$

where the parameter λ is a length scale proportional to the width of the phase-field transition. In this model, the transition represents the change of fungal cell density, which determines the aggregation of biomass in macroscopic structures. The remainder, namely $W_\phi + B_\phi$, represents the contribution of the bulk phase energy. This contribution features a symmetric double-well potential

$$W_\phi = \phi^2(1-\phi)^2, \tag{4}$$

to which we add the a bias term B_ϕ to model the asymmetric behavior related to the biological response. In the spirit of [44, 45], we define this bias term as

$$B_\phi = n(c)s(\phi), \tag{5}$$

where $n(c)$ is a nutrient bias that accounts for the increase or decrease of fungal cells due to the presence or absence of nutrients in the medium, and the function $s(\phi)$ corresponds to a seed bias. The seed bias simply ensures that fungal biomass has to be present in order to grow new cells. In their simplest form, $s(\phi)$ increases monotonically and may exhibit lower and upper thresholds. Furthermore, $n(c)$ imposes a hyperbolic tangent or similar step function to signal the growing or decaying conditions depending on the nutrient availability (top part of Fig. 3). In our model we use the following expressions for these biases

$$n(c) = \alpha \arctan[\beta\,(c - c^*)], \quad \alpha = -\frac{2}{3.01\pi}, \tag{6}$$

$$s(\phi) = \phi^2\,(3 - 2\phi)\,, \tag{7}$$

where α and β control the shape of the transition and c^* is a concentration threshold at which the growing behavior becomes possible. The effect of the bias on the free bulk energy is illustrated in Fig. 3. On the bottom-left, we plot the symmetric double-well W_ϕ (left axis) and two

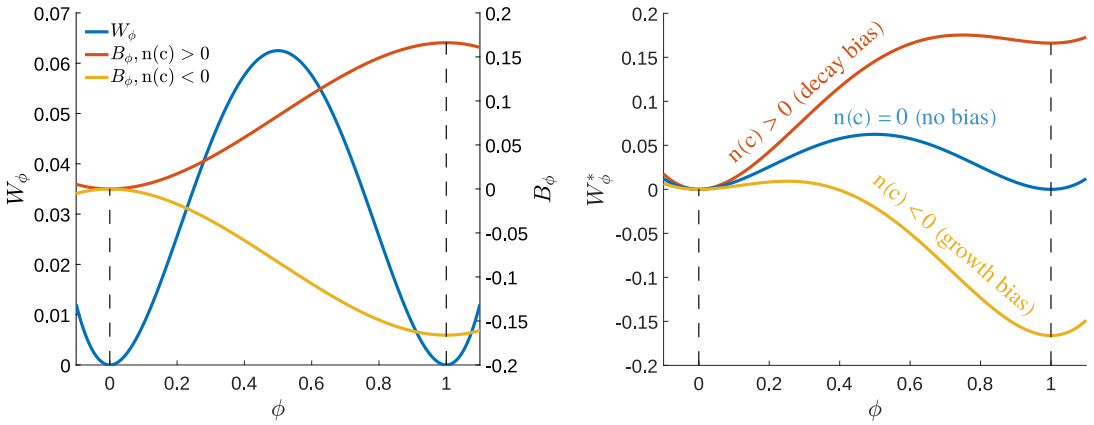

Figure 3. Left: symmetric double-well bulk energy contribution (in blue), along with nutrient positive (in orange) and negative (in yellow) biases plots in terms of ϕ. Right: case examples of the overall bulk phase free energy density, W^*_ϕ, defined as the addition of the double-well potential and the correspondent bias.

representative examples of the nutrient bias B_ϕ (right axis). When $n(c) > 0$, the B_ϕ increases toward phase $\phi = 1$ (existence of fungus), which promotes decay of the biomass by making the creation of the fungus less favorable. Conversely, $n(c) < 0$ results in a decreasing B_ϕ that penalizes phase $\phi = 0$ (absence of fungus), and consequently promotes the growth of the mycelium. This response can be further visualized on the right side of Fig. 3, where the overall free bulk energy landscape $W^*_\phi = W_\phi + B_\phi$, is presented. The presence or absence of nutrient c defines the shape of the double-well, which may have no bias, favor growth, or favor decay of biomass depending on the concentration c.

2.4. Nutrient diffusive media

Fungi in general, and Ophiocordyceps in particular, can be found embedded in media that contain the necessary nutrients for its development and support. The particular distribution of the nutrients in the medium, along with its evolution in time due to a variety of processes, determine the mycelial structure. In our case, the main processes affecting the nutrient distribution are the diffusive and advective transports, and the consumption by the fungus to survive and grow new biomass. Further phenomena can include chemical reactions in the media or inside the mycelium, through metabolism. In this work we consider diffusion as the main nutrient transfer mechanism. While the nutrient availability in Ophyocordyceps is affected by the flow of the hemolymph, we consider the flow as responsible for nutrient boundary conditions, and approximate their distribution as a process of diffusive nature. The influence of the flow in specific geometries will be studied in future work. The choice adopted herein allows one to establish comparisons with laboratory-controlled Petri dish experiments, usually happening on substrates of diffusive character. Consequently, we model the nutrient redistribution in the system composed by the fungal mycelium and the outer medium as the diffusive process

$$\frac{\partial c}{\partial t} = \nabla \cdot (M_c \nabla c) + r_s(\phi, c) - r_f(\phi), \tag{8}$$

where M_c is the nutrient mobility, and where r_s and r_f are source and fungal consumption terms. The source term r_s is just a replenishment rate that can be used to simulate an outer domain supply of nutrient in two-dimensional settings. For example,

$$r_s(\phi, c) = \tfrac{1}{4}\left[1 + \tanh\left(\gamma_\phi\left(\phi - \phi^*\right)\right)\right]\left[1 - \tanh\left(-\gamma_c\left(c - c^{\max}\right)\right)\right], \tag{9}$$

where parameters γ_ϕ and γ_c control the shape of the step functions, and thresholds ϕ^* and $c^{\max}$ establish the conditions that allow the replenishment to stay within feasible limits. More important for the model is the term of fungal consumption r_f. This term encompasses the overall nutrient consumption of the fungal biomass using two separate terms,

$$r_f(\phi) = \kappa_1\phi + \kappa_2\frac{\partial\phi}{\partial t}, \tag{10}$$

where the first term corresponds to consumption for biomass support (i.e., amount to keep the fungus alive), and the second term accounts for creation of new biomass. The parameter κ_1 is a rate (i.e., consumed nutrient per unit of time) and κ_2 as the mass ratio transformation (i.e., amount of nutrient to create a unit of fungal biomass). The mobility M_c is in general not constant, and accounts for the different media expected in the system. That is, one can expect a mobility in the hemolymph that is different from that inside the fungal mass. As such, M_c is an important factor controlling the pattern of the fungal growth. We capture this differences using the following expression:

$$M_c = 0.45\left[1 + \tanh\left(C\left(\phi - \phi^*\right)\right)\right] + 0.1, \tag{11}$$

where ϕ^* represents a threshold at which we start to modify the nutrient mobility as it enters the fungal body.

2.5. Governing equations

Given the chosen model, and using standard thermodynamic arguments, the variational derivative of the fungal free energy potential with respect to the phase-field ϕ measures the (generalized) force promoting the temporal evolution of the field ϕ. We posit that the evolution in question is point-wise "proportional" to said force:

$$\frac{\partial\phi}{\partial t} = -G_\phi\frac{\delta\Psi}{\delta\phi} \quad \Rightarrow \quad \frac{\partial\phi}{\partial t} = G_\phi\left(\nabla\cdot\left(\frac{\partial F(\phi,\nabla\phi,c)}{\partial\nabla\phi}\right) - \frac{\partial F(\phi,\nabla\phi,c)}{\partial\phi}\right), \tag{12}$$

where the "coefficient of proportionality" G_ϕ is a growth rate, characteristic of the fungal organism. That is, G_ϕ is tasked with embodying the biology of the fungal growth. Taking into account the full expression of the fungal free energy density,

$$F\left(\phi, \nabla\phi, c\right) = \tfrac{1}{2}\lambda^2\left|\nabla\phi\right|^2 + \phi^2\left(1-\phi\right)^2 + n(c)s(\phi), \tag{13}$$

Eq. (12) can be particularized to yield:

$$\frac{\partial\phi}{\partial t} = G_\phi(\lambda^2\Delta\phi - \mu_\phi(\phi, c)), \tag{14}$$

Table 1. Geometrical data and material properties.

Property	Description	Value	Unit
ϕ	Fungal marker	$0-1$	none
c	Dimensionless nutrient concentration	$0-1$	none
L	Domain size	$3.0-10$	cm
c^*	Growth nutrient threshold	0.4	none
κ_1	Consumption rate	$1.0 \cdot 10^{-1}$	$1/h$
κ_2	Growing consumption	$2.0 \cdot 10^{1}$	none
G_ϕ	Growing rate	$1.0 \cdot 10^{2}$	$1/h$
M_c	Nutrient mobility	$1.0 \cdot 10^{-1}$	cm^2/h
λ	characteristic length scale	$1.0 \cdot 10^{-2}$	cm

where $\mu_\phi = \partial F/\partial\phi$ is defined as the chemical potential associated to F. The system is completed with the evolution equation for the nutrient concentration (8). The problem then consists in finding ϕ and c such that:

$$\frac{\partial\phi}{\partial t} = G_\phi(\lambda^2\Delta\phi - \phi(4\phi^2 - 6\phi + 2) + 6(\phi - \phi^2)n(c)) \quad \text{in } \Omega \times [0, t_f], \tag{15}$$

$$\frac{\partial c}{\partial t} = \nabla \cdot (M_c \nabla c) + r_s(\phi, c) - r_f(\phi) \quad \text{in } \Omega \times [0, t_f], \tag{16}$$

subject to boundary and initial conditions

$$\phi = \phi_D \quad \text{on } \partial\Omega_D \times [0, t_f], \tag{17}$$

$$c = c_D \quad \text{on } \partial\Omega_D \times [0, t_f], \tag{18}$$

$$\nabla\phi \cdot \boldsymbol{n} = 0 \quad \text{on } \partial\Omega_\mu \times [0, t_f], \tag{19}$$

$$\nabla c \cdot \boldsymbol{n} = \boldsymbol{q}_c \quad \text{on } \partial\Omega_N \times [0, t_f], \tag{20}$$

$$\phi = \phi_0 \quad \text{in } \Omega(t = 0), \tag{21}$$

$$c = c_0 \quad \text{in } \Omega(t = 0), \tag{22}$$

where we consider Dirichlet boundary conditions on ϕ and c, a possible nutrient source or flux condition on the Neumann boundary $\partial\Omega_N$, the chemical equilibrium condition on the boundary $\partial\Omega_\mu$ for the biomass ϕ [51], and the corresponding initial conditions. In general, the boundary represents a cuticle or impenetrable wall, and hence $\phi_D = 0$ on its totality. Despite the simplicity pursued in its derivation, the model exhibits a number of parameters whose units and typical values are summarized in Table 1.

3. Discrete equations

We outline here the numerical implementation details of the phase-field model presented in Section 2. The numerical implementation was carried out by adopting a standard Galerkin finite element method (FEM). Let $X = \boldsymbol{x}^1, \boldsymbol{x}^2, \ldots, \boldsymbol{x}^N$ be a node set representing the physical domain in which the fungal network propagates. We define in this domain the associated finite

element (FE) first-order polynomials basis functions, denoted as $p_a(\boldsymbol{x}), a = 1, \ldots, N$. Consider also a set of quadrature points $\hat{X} = \hat{\boldsymbol{x}}^1, \hat{\boldsymbol{x}}^2, \ldots, \hat{\boldsymbol{x}}^Q$ and the associated quadrature weights $W = w^1, w^2, \ldots, w^Q$. Under this assumptions, we can then interpolate the values and gradients of the phase-field variable $\phi(\boldsymbol{x})$ and concentration variable $c(\boldsymbol{x})$ as:

$$\phi(\boldsymbol{x}) = \sum^{a} p_a(\boldsymbol{x})\phi_a, \quad \nabla\phi(\boldsymbol{x}) = \sum^{a} \boldsymbol{b}_a(\boldsymbol{x})\phi_a, \tag{23}$$

$$c(\boldsymbol{x}) = \sum^{a} p_a(\boldsymbol{x})c_a, \quad \nabla c(\boldsymbol{x}) = \sum^{a} \boldsymbol{b}_a(\boldsymbol{x})c_a, \tag{24}$$

where $p_a(\boldsymbol{x})$ and $\boldsymbol{b}_a(\boldsymbol{x})$ correspond to the traditional scalar and vector expressions for linear FEM shape functions and their gradients (i.e., $\boldsymbol{b}_a = \nabla p_a$), and the nodal coefficients of the interpolation they describe are denoted by ϕ_a, c_a. Following a Galerkin approach, we use the same interpolating functions to define the test functions $\delta\phi$ and δc used in the variational form of the equations.

3.1. Spatial discretization

We construct our variational framework starting from Eqs. (15) and (16), and multiplying them by the test functions $\delta\phi_i$ and δc_i, respectively. We integrate by parts over the domain Ω and then discretize with linear FEM shape functions. Term by term, the discretized weak form of the evolution equations take the following form.

3.1.1. Fungal evolution discretization

We start with the temporal part of Eq. (15), which can be expressed and discretized as

$$\int_\Omega \frac{\partial\phi}{\partial t}\delta\phi_i \; d\Omega = \sum^{nel}\sum^{nq}\sum^{a} p_a(\boldsymbol{x})\dot{\phi}_a p_i(\boldsymbol{x})\omega_q, \tag{25}$$

where the generic summatories over the number of elements nel and the number of quadrature points per element nq have been introduced, and i is an index for the test function. The right hand side of the fungal balance evolution, corresponding to the variation of the free fungal energy density with respect to ϕ, yields

$$\int_\Omega G_\phi(\lambda^2\Delta\phi)\delta\phi_i \; d\Omega - \int_\Omega \left(\phi(4\phi^2 - 6\phi + 2) + 6(\phi - \phi^2)n(c)\right)\delta\phi_i \; d\Omega. \tag{26}$$

In detail, the interface term discretization becomes

$$\int_\Omega \lambda^2 G_\phi\Delta\phi\delta\phi_i \; d\Omega = -\int_\Omega \lambda^2\nabla(G_\phi\delta\phi_i)\nabla\phi \; d\Omega + \int_{\partial\Omega} \lambda^2(G_\phi\nabla\phi \; \boldsymbol{n})\delta\phi_i \; d\partial\Omega, \tag{27}$$

$$\int_\Omega \lambda^2\nabla(G_\phi\delta\phi_i)\nabla\phi \; d\Omega = \lambda^2\sum^{nel}\sum^{nq}\left(\nabla G_\phi p_i(\boldsymbol{x}) + G(d)\nabla p_i(\boldsymbol{x})\right)\sum^{a}\boldsymbol{b}_a(\boldsymbol{x})\phi_a\omega_q. \tag{28}$$

The final term, corresponding to the bulk contribution, takes the form:

$$\int_\Omega (\phi(4\phi^2 - 6\phi + 2) + 6(\phi - \phi^2)n(c))\delta\phi_i \; d\Omega = \tag{29}$$

$$\sum^{nel}\sum^{nq}\left[\left(\sum^{a}p_a(\boldsymbol{x})\phi_a\right)\left(4\left(\sum^{a}p_a(\boldsymbol{x})\phi_a\right)^2-6\left(\sum^{a}p_a(\boldsymbol{x})\phi_a\right)+2\right)\right.$$
$$\left.+6\left(\sum^{a}p_a(\boldsymbol{x})\phi_a-\left(\sum^{a}p_a(\boldsymbol{x})\phi_a\right)^2\right)n(c)\right]p_i(\boldsymbol{x})\omega_q. \tag{30}$$

3.1.2. Nutrient evolution

We start from the variational form of the nutrient evolution Eq. (16), which can be written as

$$\int_\Omega \frac{\partial c}{\partial t}\delta c_i\ d\Omega=\int_\Omega \nabla\cdot(M_c\nabla c)\,\delta c_i\ d\Omega+\int_\Omega r_s(\phi,c)\delta c_i\ d\Omega-\int_\Omega r_f(\phi)\delta c_i\ d\Omega. \tag{31}$$

As before, the temporal derivative can be discretized in space following

$$\int_\Omega \frac{\partial c}{\partial t}\delta c_i\ d\Omega=\sum^{nel}\sum^{nq}\sum^{a}p_a(\boldsymbol{x})\dot{c}_a p_i(\boldsymbol{x})\omega_q, \tag{32}$$

and the diffusive component leads to the terms

$$\int_\Omega \nabla\cdot(M_c\nabla c)\,\delta c_i\ d\Omega=-\int_\Omega M_c\nabla c\nabla\delta c_i\ d\Omega+\int_{\partial\Omega}(M_c\nabla c\ \boldsymbol{n})\delta c_i\ d\partial\Omega. \tag{33}$$

When discretized, the bulk domain contribution yields the expression

$$\int_\Omega M_c\nabla c\nabla\delta c_i\ d\Omega=\sum^{nel}\sum^{nq}\sum^{a}M_c\boldsymbol{b}_a(\boldsymbol{x})\boldsymbol{b}_i(\boldsymbol{x})c_a\omega_q. \tag{34}$$

Finally, the discretization of the source and consumption terms can be written as:

$$\int_\Omega r_s(\phi,c)\delta c_i\ d\Omega=\sum^{nel}\sum^{nq}r_s\left(\sum^{a}p_a(\boldsymbol{x})\phi_a,\sum^{a}p_a(\boldsymbol{x})c_a\right)p_i(\boldsymbol{x})\omega_q, \tag{35}$$

and

$$\int_\Omega\left(\kappa_1\phi+\kappa_2\frac{\partial\phi}{\partial t}\right)\delta c_i\ d\Omega=\sum^{nel}\sum^{nq}\left(\kappa_1\sum^{a}p_a(\boldsymbol{x})\phi_a+\kappa_2\sum^{a}p_a(\boldsymbol{x})\dot{\phi}_a\right)p_i(\boldsymbol{x})\omega_q, \tag{36}$$

where $\dot{\phi}_a$ represents the time derivative of the corresponding nodal coefficient.

3.2. Time discretization

To discretize Eqs. (15) and (16) we adopt a standard second order backward difference formula (BDF) formula, which is A-stable. The BDF2 algorithm is applied to our PDEs in the form $\partial d/\partial t=f(d,\nabla d,t)$:

$$\int_\Omega\left(\frac{\frac{3}{2}d^{n+1}-2d^n+\frac{1}{2}d^{n-1}}{\Delta t}-f(d^{n+1},\nabla d^{n+1})\right)\delta d_i\ d\Omega=0. \tag{37}$$

This form can be directly applied to our nonlinear system of equations. Note that two initial steps are required in this type of algorithm (two solutions for previous points in time). The requested additional guess can be computed using a first order technique (e.g., a Backward Euler scheme solution). This strategy can be generalized for the variable time stepping we use in our simulations by using the following definition of the discretized time derivative:

$$\frac{\partial d}{\partial t} = a_1 d^{n+1} - a_2 d^n + a_3 d^{n-1},$$
$$a_1 = \frac{2\Delta t^{n+1} + \Delta t^n}{\Delta t^{n+1}(\Delta t^{n+1} + \Delta t^n)}, \quad a_2 = -\frac{\Delta t^{n+1} + \Delta t^n}{\Delta t^{n+1}\Delta t^n}, \quad a_3 = \frac{\Delta t^{n+1}}{\Delta t^n(\Delta t^{n+1} + \Delta t^n)}. \tag{38}$$

The simulations in this paper have been obtained using constant time stepping (for comparison in the model testing) and a DT2 adaptive time stepper based on a global time discretization relative error estimate e_n, which can be computed as:

$$e_n = \frac{\hat{e}_n}{\Delta t^n}, \qquad \hat{e}_n = \frac{||d^{n+1} - \hat{d}^{n+1}||}{max(||d^{n+1}||, ||\hat{d}^{n+1}||)}). \tag{39}$$

When e_n is above a tolerance e_{max}, the algorithm shrinks the step size. Otherwise, the time step is updated following the rule $\Delta t^{n+1} = \Delta t^n \left(e_{tol}/e_n\right)^{1/p}$, where e_{tol} is a tolerance and p is the global convergence rate of the scheme.

4. Numerical examples: model testing and validation

In this section, we present numerical results to illustrate and test the behavior of the model presented in Section 2. The discretized equations developed in Section 3 have been implemented following efficient high performance strategies [52] in the partially open-source software Multiphysics Object-Oriented Simulation Environment (MOOSE), developed primarily at Idaho National Lab [53]. Results regarding convergence are presented first. Subsequently, the parameter space and the capacity of the model to represent different behaviors and structure patterns is explored. A first illustrative example of the model behavior is presented in Fig. 4. In this simple setting, a fungal seed is placed at the bottom-center of the rectangular domain shown in Fig. 4(right). The presence of a uniform quantity of nutrient stimulates the growth of the mycelium, which advances in a specific pattern. The pattern is dictated by interaction between the different parameters describing the fungus and environment. Magnification on Fig. 4 emphasizes the smooth transition resulting from the phase-field approach, which profile has been plotted on the left side of the figure.

4.1. Model convergence results

We test here the reliability of the solutions obtained with the model as the mesh is refined. We also investigate the influence of the relation of the length scale represented by λ with the mesh size. We start analyzing the mesh sensitivity of the total fungal biomass and maximum bulk free energy for a problem with similar characteristics to the one in Fig. 4, where a seed of fungus develops into a full structure and then slightly decays until reaching equilibrium. Uniform and adaptive mesh and time-stepping schemes are used to simulate the development

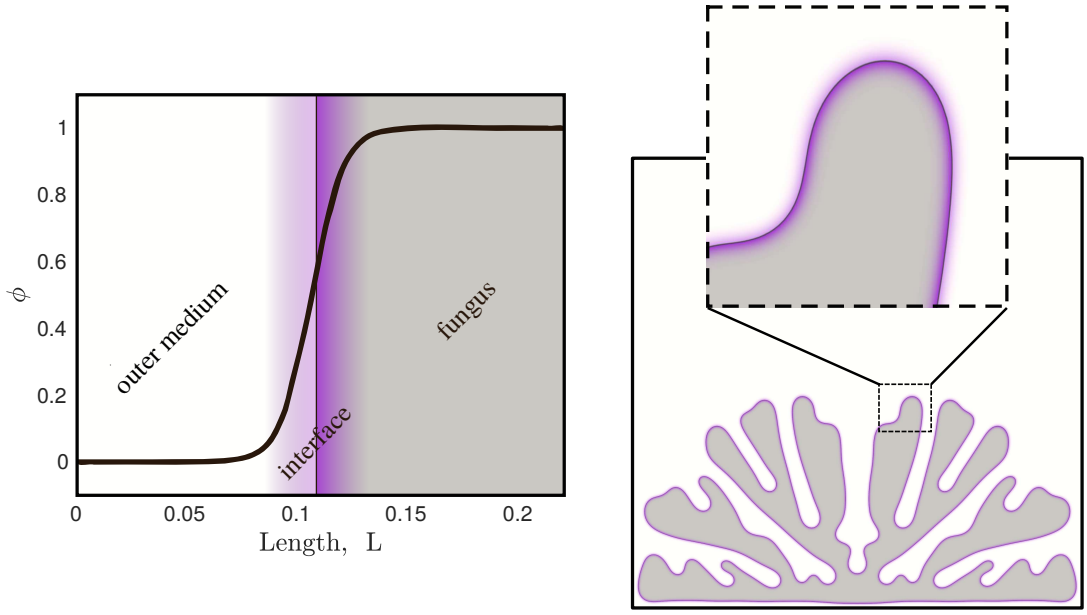

Figure 4. Illustration of a fungal phase-field model simulation. The fungus seed, placed at the center of the bottom edge, develops in a uniformly distributed nutrient domain.

Table 2. Convergence with decreasing element size. Corresponding values of the maximum amount of mass and free energy to λ/h_{min} are tabulated, where λ is the length scale and h_{min} is the minimum element size.

Mesh	h_{min}	λ/h_{min}	Fungal Biomass	Free Energy
AQM1	$3.125 \cdot 10^{-2}$	0.32	10.4980	0.4519
AQM2	$1.562 \cdot 10^{-2}$	0.64	9.6658	0.3782
UQM1	$1.172 \cdot 10^{-2}$	0.85	9.0453	0.3269
UQM2	$9.375 \cdot 10^{-3}$	1.07	8.6883	0.2983
AQM3	$7.812 \cdot 10^{-3}$	1.28	8.4543	0.3102
ATM1	$6.650 \cdot 10^{-3}$	1.50	8.5970	0.2958
AQM4	$3.906 \cdot 10^{-3}$	2.56	8.5466	0.2906
ATM2	$3.630 \cdot 10^{-3}$	2.75	8.4331	0.2900

using gradually higher levels of refinement. Some of these results have been compared against equivalent uniform time-stepping to ensure correctness. Table 2 summarizes the results for the different types of mesh, labeled with a "XYM" code plus an identifying number. In the label, "X" can become "U" for uniform or "A" for adapted. Likewise, "Y" can be "T" for triangular or "Q" for quadrilateral. The smallest element size h_{min} and its λ/h_{min} ratio are given in the second and third columns. Fourth and fifth columns display the overall domain aggregate of fungal biomass (ϕ) and fungal bulk energy W^*_ϕ. The results suggest the gradual convergence of both mass and energy for the point of maximum development of the fungal pattern, which is the most unfavorable point for comparison, since the problem is highly non-linear and time dependent. Further insight into the convergence of the whole evolution in time is reported in

Fig. 5, for both the free energy (left) and the mass (right). As can be observed, the final relaxed pattern is clearly off when $\lambda \leq 0.7h_{min}$. We recall here that λ is a length scale related to the interface width, which in this case corresponds approximately to $2.0h_{min}$, a consistent result with classical resolution requirements in phase-field methods [43, 54]. Beyond this point, the final patterns are gradually convergent and the shapes become quickly indistinguishable. However, we report that a higher level of refinement seems to be required for the convergence in full along the process. We report that meshing with ratios $\lambda \geq 2h_{min}$ give rise to almost coincident paths. In study cases where the mycelium evolution in time is of importance, aside from obtaining the final equilibrium shape, these levels of refinement should be considered. Notice the connection between the converging plots presented in Fig. 5 and their λ/h_{min} ratio in Table 2, which makes clear the effect that this value has in the growing process. Moreover, we provide in Fig. 6 a visual comparison for the processes corresponding to the meshes $AQM1$, $AQM2$, $AQM3$, and $AQM4$, at their largest development point. The comparison provides a qualitative measure, beyond the data presented in Table 2, of the convergence of the phase-field patterns obtained as the mesh is refined in relation with the length scale λ. The structures obtained, even in this non-relaxed point, start to be reliable from $\lambda = 1.28h_{min}$, and converge towards an almost coincident shape when $\lambda \geq 2h_{min}$.

4.2. Effect of nonuniform nutrient distributions and boundary conditions

In this section, we test the capabilities of our model to reproduce phenomena such as growth, death, and migration in reaction to variable nutrient availability, and how different initial and boundary conditions interact with the mycelium, modifying its response. In Fig. 7, we show three time snapshots for a pair of simulations of fungal growth in the presence of a nutrient gradient, with different positions for the initial seed. This initial seed is modeled as a small circle, and no significant changes are observed when small variations to its radius are introduced. In both simulations, the size of the domain is set to $L = 10\,\text{mm}$, the maximum refinement is $\lambda = 6h$, and the nutrient concentration c varies linearly from a normalized maximum of 1 on the left wall to 0.5 on the right wall. No replenishment source is applied in this case. In the simulation at the top of Fig. 7, the initial seed is placed at the bottom-left corner. In the bottom simulation, the seed can be found at the bottom-center of the domain. Under the same nutrient gradient, both cases show the fungus favoring first the zone with higher nutrient concentrations. However, the seed located the corner is inside the nutrient abundant zone, and hence experiences a rapid fined branched expansion in the vertical direction. The case is different for the seed at the bottom-center, which pattern develops in thicker branches and towards the left, to the higher concentration area. Notice also that the time scale in which this happens is considerably larger. After the consumption of the more nutritious source, the fungi expand towards the less dense nutrient source (i.e., in the $-\nabla c$ direction). The absence of nutrient replenishment subsequently determines a change to a structure which is more efficient in redistributing the current nutrient resources.

In the last snapshot,the amount of nutrient is not sufficient for the fungi's front to branch out and advance, and the progression stops (part (c) of Fig. 7. During some time, there is still enough nutrient for the fungus to survive (i.e., $c \geq c^*$ in Eq. (6)), and the system reaches a pseudo-equilibrium state. Observe also that some of the fungal biomass on the left side of the domain disappears, as it cannot be further sustained.

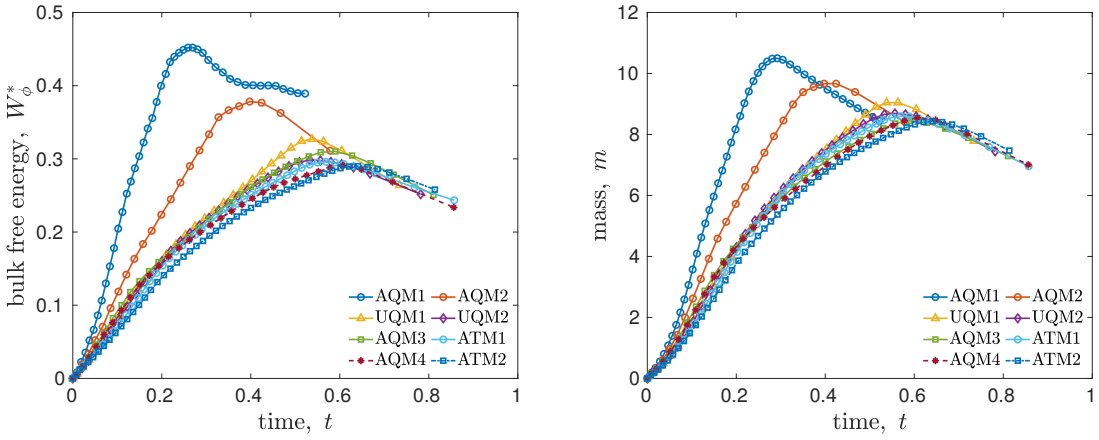

Figure 5. Evolution in time (days) of the bulk free energy (a) and fungal biomass (b) for different mesh sizes, labeled as presented in Table 2. The amount of fungal biomass decreases after a peak in value that signals the initiation of the decaying phase due to the depletion of nutrients in the system.

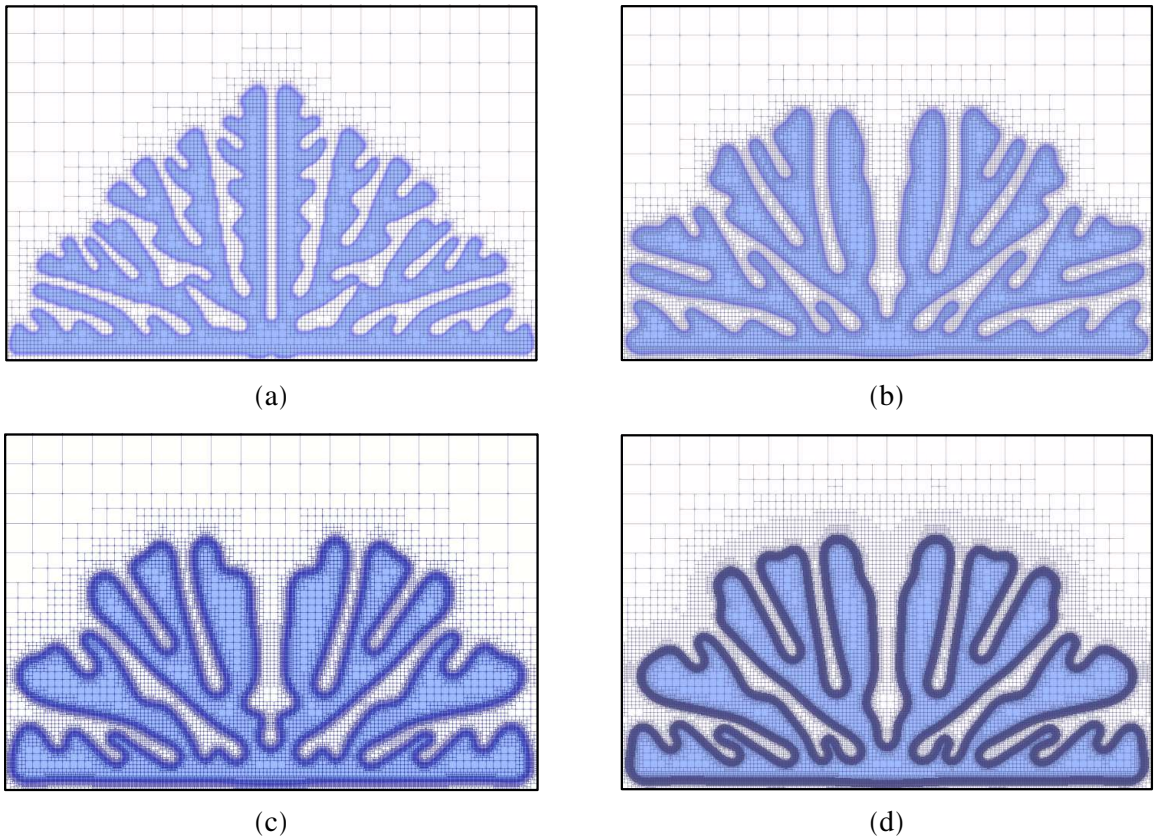

Figure 6. Convergence of ϕ shape as the mesh is progressively refined for (a) $\lambda = 0.32h_{min}$, (b) $\lambda = 0.64h_{min}$, (c) $\lambda = 1.28h_{min}$, (d) $\lambda = 2.56h_{min}$.

Growth, decay, and migration phenomena are further illustrated by testing the model with a new set of boundary conditions. In Fig. 8, we have introduced a constant nutrient source at the top edge. The seed is placed ant the bottom-center of the domain (a). As can be observed in the sequence of snapshots, the fungus develops in exploratory way due to the initial uniformity of the nutrient already present. As the nutrient is consumed, the fully developed fungus migrates towards the only source of nutrient, while decays and finally disappear at the bottom zone. This transition, which starts in (b), finishes with the full colonization of the source edge, which is able to sustain now a uniform band of fungal biomass (c). The thickness of this band depends on the parameters of the problem, such as the nutrient mobility and the fungus nutrient consumption rate. This aspect is analyzed in the next section.

4.3. Parameter space analysis and morphologies

As pointed out in Section 2, and perceptible in the previous examples, the model response is sensitive to a considerable amount of parameters, which describe fungus and outer medium. In this section, we pursue a better understanding of the model capabilities to generate different patterns and network structures. We conduct a parametric study to identify the relevant dimensionless quantities that dictate the behavior of the mycelium, and the ranges in which they play a significant role. The results of this study suggest that the behavior of the system is linked to

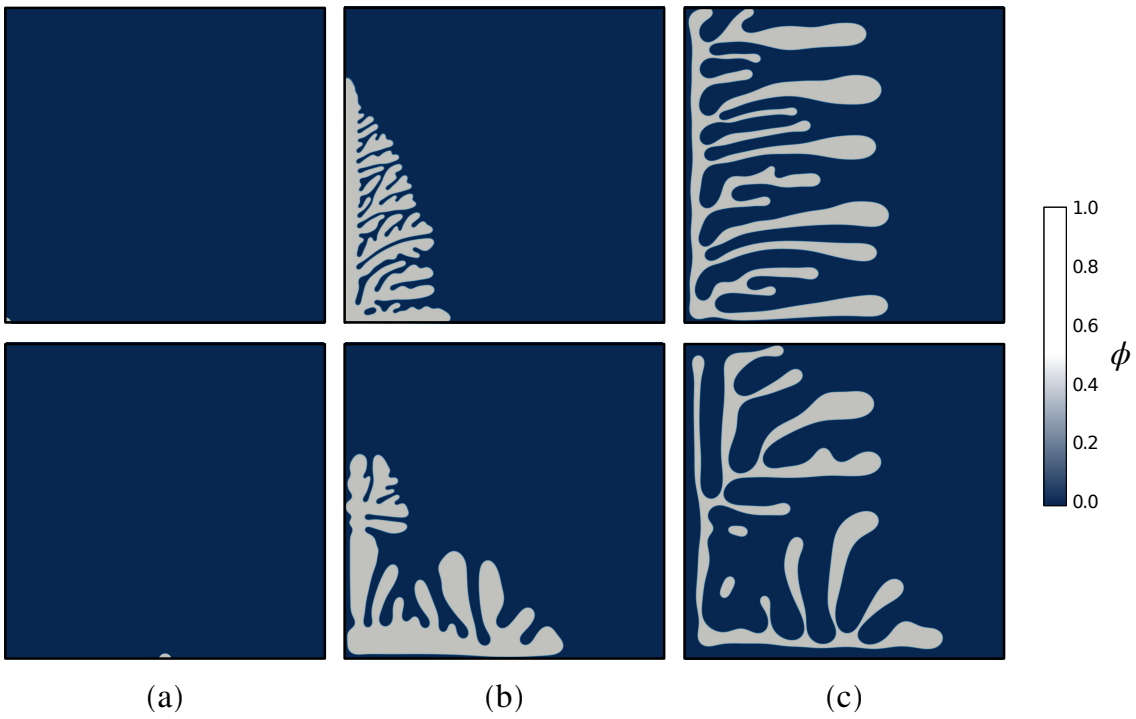

Figure 7. Evolution of ϕ in the presence of a nutrient gradient. Nutrient source linearly decreases from the left to the right boundary wall. Top: (a) Fungus seed at the bottom-left corner at $t = 0$, (b) Snapshot at $t = 0.332$, (c) System reaches an equilibrium state at $t = 5.187$. Bottom: (a) Fungus seed at the middle of the bottom edge at $t = 0$, (b) Snapshot at $t = 1.769$, (c) System reaches an equilibrium state at $t = 9.744$. Time here is in hours.

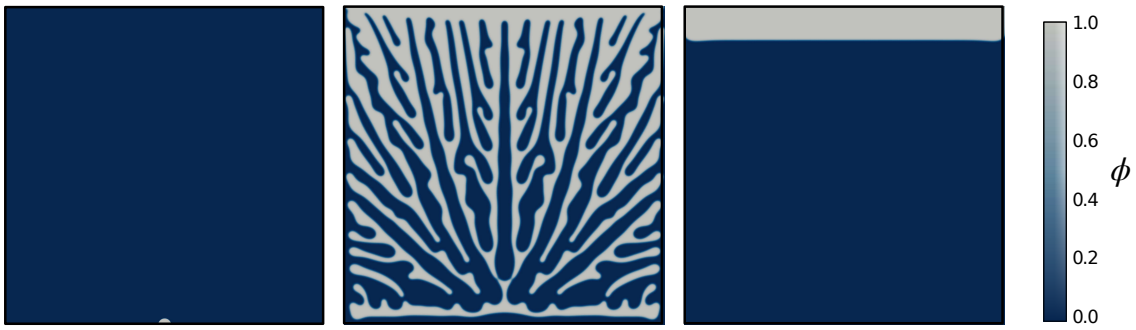

Figure 8. Evolution of ϕ in the presence of a constant nutrient source. The constant nutrient source is placed on the top boundary. (a) Fungus seed at the middle of the bottom edge at $t = 0$, (b) Snapshot at $t = 0.213$, (c) Fungus stabilizes at the top edge where there is a constant supply of nutrient at $t = 0.946$. Time here is in days.

three dimensionless numbers. The first two numbers are described by the relations κ_1/M_c^* and G_ϕ/M_c^*, where $M_c^* = M_c/L_0^2$ corresponds to a nutrient mobility that has been normalized by the domain's characteristic length L_0. The third number is κ_2, which is already dimensionless in this framework, as mass is represented by the phase-field. The interpretation of these quantities and their influence in the network development becomes clear when exploring the associated parameter space, shown in Figs. 9 and 10.

The effect of κ_2 and G_ϕ/M_c^* on the evolution of the fungal structure is shown in Fig. 9. Each one of the pictures in the matrix arrangement corresponds to the same instant in dimensionless time $t^* = t/\tau_\phi$, where $\tau_\phi = 1/G_\phi$ is a characteristic time of the fungus, with dimensionless parameters that vary according to the horizontal (G_ϕ/M_c^*) and vertical axes (κ_2). In this space, the number G_ϕ/M_c^* appears as the relevant one regarding the overall structure shape of the network. This number can be interpreted as the competition of the fungal growth rate and the velocity at which nutrients redistribute in the system. As this value increases, a variety of branching patterns are observed, ranging from circular growing when nutrient is always in abundance (the fungus is slow, or the fungus/media is efficient in redistribution), to branching structures with highly complex connectivity blueprints (fungus is fast, or nutrient cannot be efficiently redistributed, forcing an intermediate scale network).

Based on the changes observed in the vertical axis, we reinterpret κ_2 as a development number, which controls the spacing between the branches. This shows that higher consumption for growing new cells leads to insufficient nutrient levels in the vicinity of existing branches, limiting the growth of new ones. Conversely, lower values of κ_2 are conducive to denser, fuller structures. In conclusion, as we move from left to right we have similar amount of mass with increasing level of branching, while moving top to down we have a similar pattern with an increasing developed structure that has presents more fungal biomass.

To complete this three-dimensional parameter space, Fig. 10 illustrates the role of the number κ_1/M_c^*. We keep fixed the other parameters and test the response of the fungus to changes in

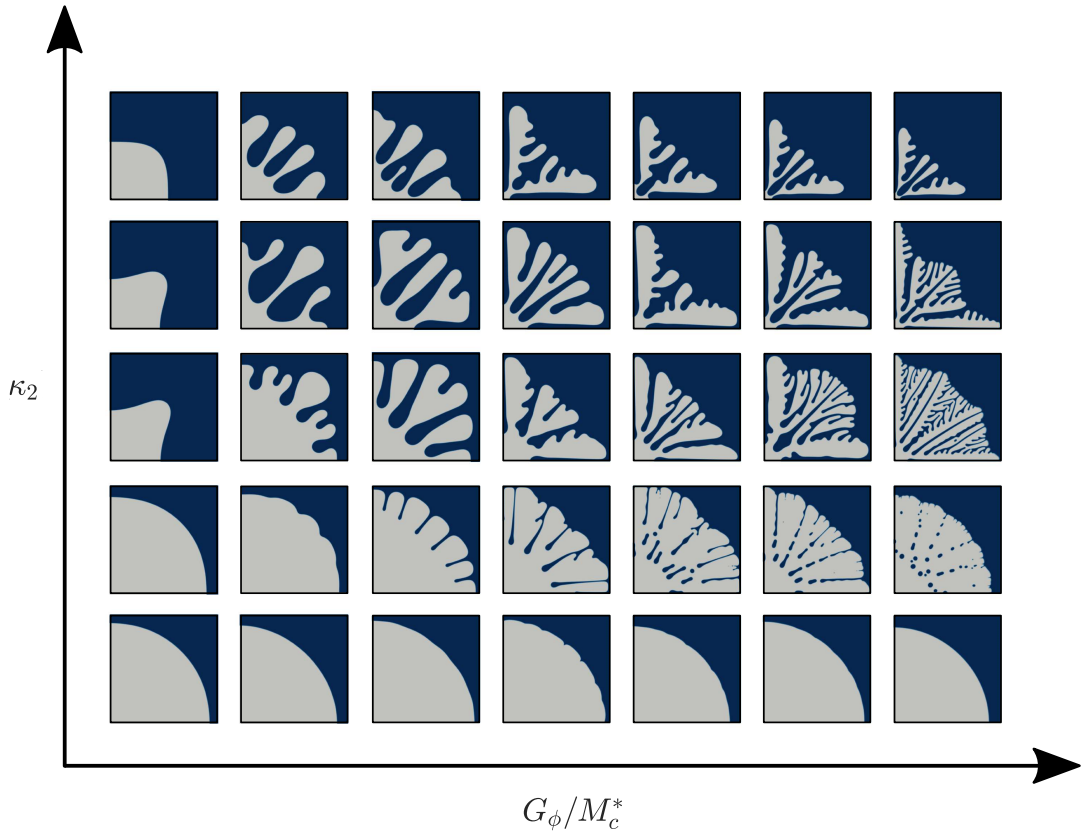

Figure 9. Parameter space corresponding to values G_ϕ/M_c^* and κ_2. The overall complexity of the structure is increased in the horizontal axis. The vertical axis controls the spacing between the branches.

the value of κ_1. For comparison purposes, we label the snapshots with $\kappa_1^* = \kappa_1/\kappa_1^{ref}$, being $\kappa_1^{ref} = 0.1$ the value of κ_1 in the first pattern. The sequence shows that this parameter controls the thickness of the branches, as the ratio can be interpreted as a competition between the consumption rate of the existing fungal cells and the available redistributed nutrient. In plain words, a higher consumption leads to a diminished capacity to sustain highly massive networks.

Interestingly, a closer look at the Fig. 9 reveals that the proposed model is capable of capturing well-established fungal colony morphology patterns. These patterns, observed and classified in the bacteriology literature [55], are discernible via the aggregate shape and via the margin of the colony. Without changing the nutrient conditions, we tune the fungus descriptive parameters and illustrate some of the most typical patterns in Figs. 11 (aggregate shape) and 12 (colony margin). Aggregate shapes include circular, irregular, filamentous, and rhizoid. In the colony edge department, morphologies such as entire, undulate, filiform, curled, and lobate are reproduced by the model. As we show in the next section, fungi show intermediate scale morphology switching depending on the environment. Therefore, some media heterogeneities can contribute to changes in the network morphology, which can be also captured by tuning medium parameters in our model.

5. Numerical examples: applications

We complete the model presentation by exploring the capacity of our formulation to capture phenomena that are hypothesized to happen during Ophiocordyceps network development. We qualitatively compare our results with experiments in literature performed over fungi in analogous conditions. We demonstrate the suitability of this formulation to predict growing patterns in constrained interactive networks, and its relevance to study Ophiocordyceps and similar fungal organisms.

5.1. Mycelium growth: space and time scales

In the first example, we explore the ability of our model to closely reproduce the general morphology and time scale for a given mycelium. For this purpose, we set our eyes on the time-lapse footage of the growing fungus [56]. This fungus extends its mycelium following a filiform morphology, which can be characterized by the mass (i.e., covered area), and its margin advancing rate. To reproduce this behavior, we tune our parameter values in the range indicated in the table 1. The growing consumption parameter, κ_2, is set to 0.8. Although we lack some information on the experimental conditions, it seems reasonable to choose the boundary conditions to be the same as the ones we described in section 2.5. We then proceed to simulate the evolution of the mycelium by letting the fungus seed grow from the middle of the bottom edge with a uniform nutrient concentration in the domain. As shown in Fig. 13, it can be observed that the mycelium growth pattern and development rate from our model closely mimics the one seen in the time-lapse footage. On the right side of Fig. 13, we show the overall

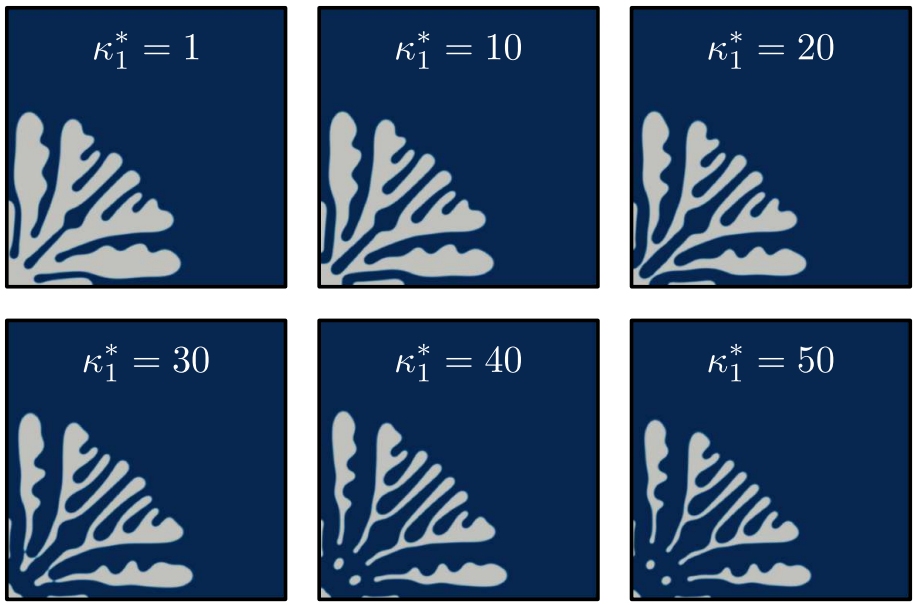

Figure 10. Parameter space corresponding to κ_1/M_c, which controls the thickness of the branches. Snapshots are labeled with a normalized κ_1^*. In the simulation, the nutrient is not replenished, leading to decay in the bottom-left corner.

filiform pattern of the simulation. The magnified section focuses on the margin of the colony, which is compared with the experiment.

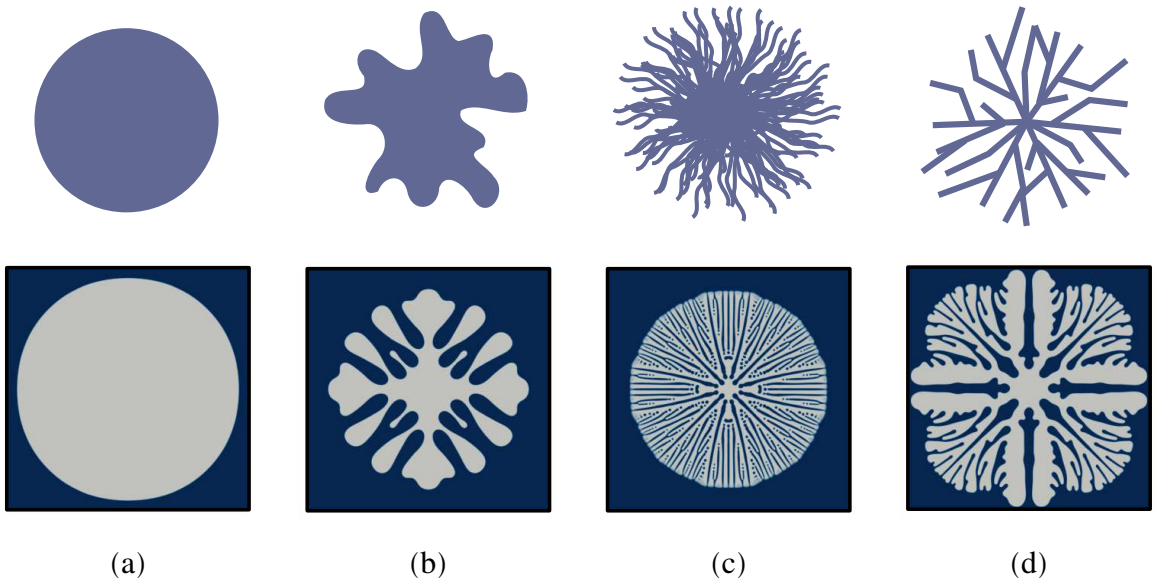

Figure 11. Comparison for the overall shape patterns in fungal colonies. Top: classical morphologies sketches (a) Circular, (b) Irregular, (c) Filamentous, (d) Rhizoid. Bottom: computational equivalent for the presented morphologies.

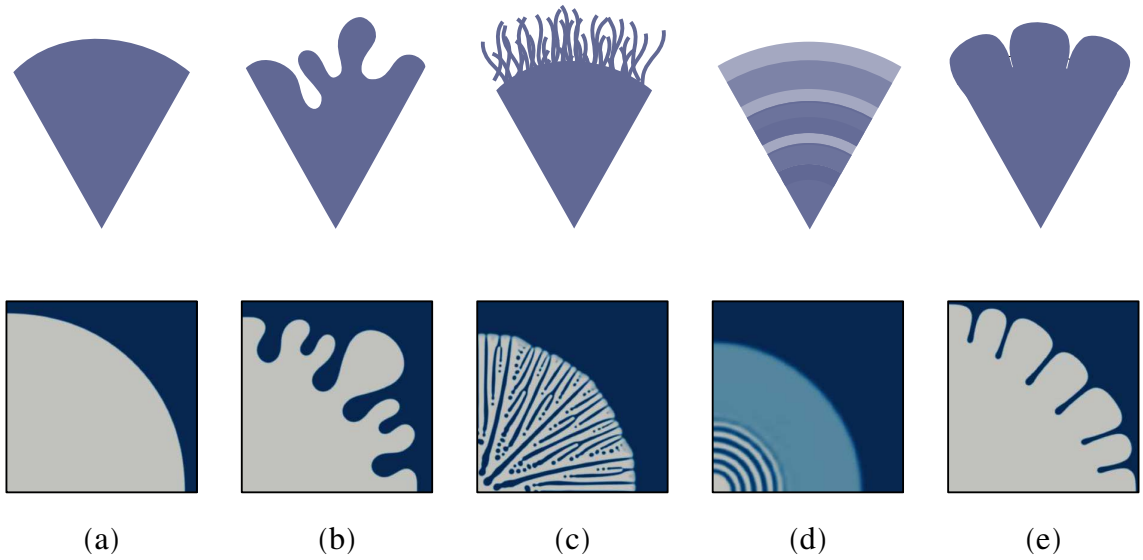

Figure 12. Comparison for the margin patterns in fungal colonies. Top: classical morphologies sketches (a) Entire, (b) Undulate, (c) Filiform, (d) Curled, (e) Lobate. Bottom: computational equivalent for the presented morphologies.

We emphasize here that the our model operates on the intermediate scale, and therefore the length scale does not necessarily account for individual hypha. In fact, each one of the branches seen in the experiment contains an aggregate of many hyphae, which build the intermediate filiform structure. A proper way to evaluate the resemblance is by qualitatively assessing the morphology (filiform) and then study a quantity of interest. In terms of structure, a quantity of interest is the produced biomass. This information can be extracted from experiment snapshots as a covered area percentage, through an image analysis procedure. An example of a post-processed image is shown in the bottom-right corner of Fig. 13. A comparison between experiment and simulation covered area indicates absolute errors around 5%. Regarding time scale, the series of images on the left of Fig. 13 compares the evolution of the mycelium margin from the experiment with that from the simulation. On every snapshot, the simulation and the experiment are superposed, showing three bands that present only simulation (left), only experiment (right), and the overlap of both (center). It is concluded from the results that our model is able to capture the overall growth pattern of the mycelium with a similar time scale observed in the experiment.

5.2. Morphology switching: concentrated nutrient source

In this example, we explore the interactivity of the network by placing concentrated nutrient sources in the medium. As we pointed in in Section 4.3, the model suggests that strong changes in the environment can induce changes in the growing patterns of the mycelium. To test this morphology switching, we take inspiration from the growth of the Physarum Polycephalum [8] in

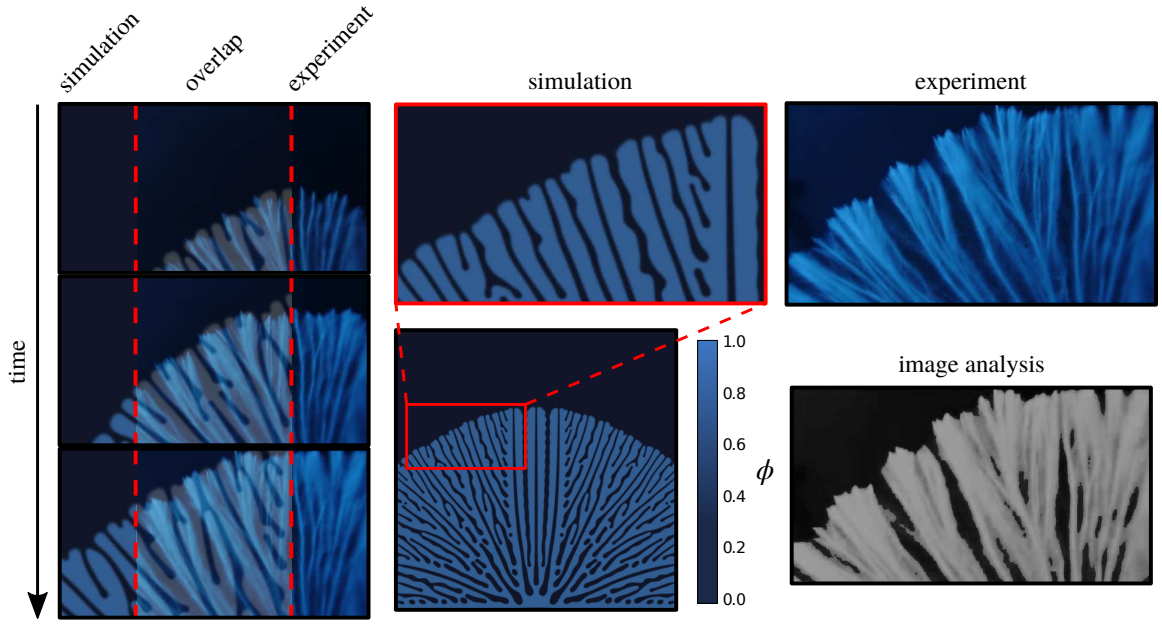

Figure 13. Simulation and experiment comparison. Right: phase-field result captures the filiform mycelium. Magnified section shows colony margin. Simulation and experiment present similar structure and area coverage. Left: simulation and experiment overlap over time. The model captures the growing time rate of the laboratory counterpart. Reproduced and adapted from [56] with kind permission of the author.

the presence of an oat kernel. Interestingly, this organism presents a very clear change of behavior when suddenly finds an abundance of nutrient, swtiching from a filiform-rhizoid network to a circular one. The circular pattern is precisely suggested by the model in abundance of resources. This type of concentrated sources can arise in the environment of Ophiocodyceps, as hemolymph circulation and muscle structures can provide similar nutrient scenarios. To mimic a time-lapse evolution of Physarum Polycephalum, we set the model parameters and boundary conditions to the ones from Section 5.1, with the addition of an elliptical concentrated nutrient source to represent the oat kernel. We assumed that the nutrient concentration for the oat kernel is twice as high as the rest of the domain, hence we set $c = 2$ for the oat kernel and $c = 1$ everywhere else.

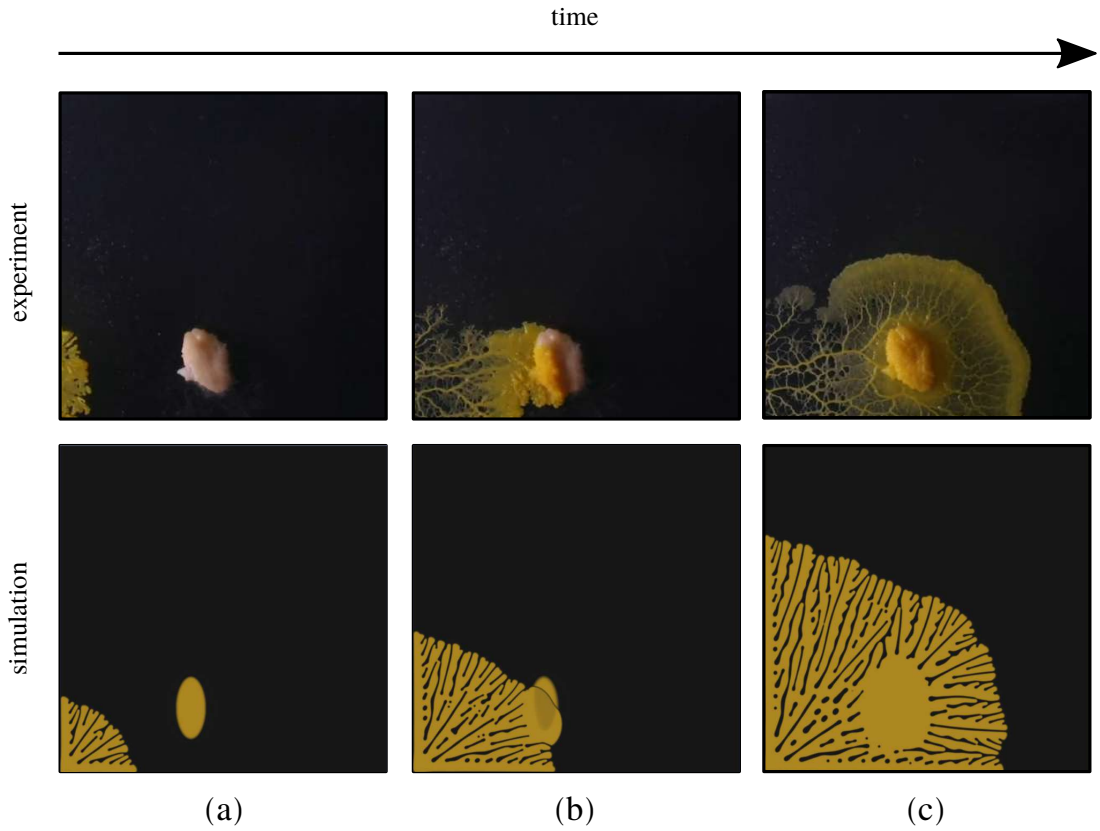

Figure 14. Morphology switching due to concentrated nutrient source. Top: Physarum Polycephalum network advances in the presence of a concentrated oat source. The abundance of nutrient induces a local circular pattern. Bottom: phase-field solution for the simulation, able to reproduce the morphology change. Reproduced and adapted from [57] with kind permission of the author.

Figure 14 shows a set of three snapshots comparing the evolution of the Physarum Polycephalum near an oat kernel in Petri dish with our simulation results. We observe in Fig. 14(a) that, similar to the experiment, the network moves toward the oat kernel in an exploratory fashion. In the second snapshot, labeled as (b), the density of the network increases on and around the oat kernel, triggering a switch of structure, that becomes circular. While the abundance

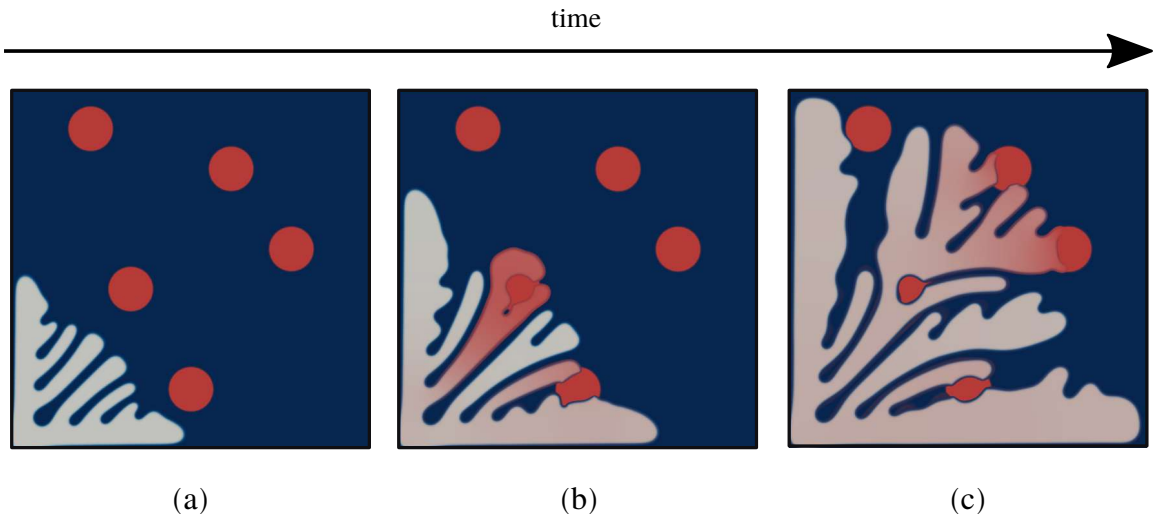

Figure 15. Agent extraction and redistribution. A rhizoid shaped network (in white) develops in the media and interacts with biomass pockets containing an agent (in red). The phase-field solution shows the extraction and redistribution process within the network.

of nutrient is present, the colony margin keep advancing in a circular pattern. This feature is captured by our model, as shown in the middle of the bottom row of Fig. 14. In snapshot (c), the network structure completely colonizes the oat source and moves past it, leaving the footprint of this circular growth event on the network, that returns to its original growth pattern. Again, this second switch is well mimicked by our formulation.

5.3. Nutrient extraction and network redistribution

When Ophiocordyceps invades the host's body parts, mainly the mandibles, it is thought to do so by forming a network that attaches to the muscle fibers, extracting and redistributing critical agents for its development. Therefore, it is essential to capture the capacity of the fungus to communicate across the network, and transport agents available in the hemolymph and inside the host cells. These agents can be used to grow, but they may have different nature. In this example we demonstrate the ability of our model to simulate the extraction and redistribution of an agent that is not immediately consumed. This new agent is represented by an additional variable, denoted by η. The variable η is governed by a diffusion equation, $\frac{\partial \eta}{\partial t} = \nabla \cdot (D_\eta \nabla \eta)$, where $D_\eta = \gamma \left(0.5 \left[\tanh\left(60\left(\phi - \hat{\phi}\right)\right) + 1\right]\right)$ is the diffusivity and we chose γ and $\hat{\phi}$ to be 30 and 0.1, respectively. We note that the expression for D_η limits the diffusion of the nutrient η to the existence of fungal marker ϕ. This is to ensure that η does not diffuse into the surrounding medium prior to the arrival of the fungus, simulating a closed container. Furthermore, we decreased the growing rate of the fungus, G_ϕ, at the boundary of η to simulate the resistance of the muscle cell to the penetration of the fungus. Full penetration inside the cells is never observed in experiments. We set $\kappa_2 = 1$ to achieve a wider spacing between the branches compared to the previous examples, better resembling the density of the network of Ophiocordyceps. Finally, we define the initial and boundary conditions to be the same as in

the other examples in this section. Figure 15 shows the evolution of the fungal network in the presence of the biomass containing agent η, represented here by red circles. We see that the fungal network grows in an exploratory fashion before reaching the agent sources in (a). Figure 15(b) shows the first encounter of the fungal network with the muscle cell. We observe that, due to the decrease in G_ϕ at the boundary of η, the fungus does not penetrate the agent pocket. Rather, it curls around the source while extracting the nutrient and diffusing it within the network. This is, in fact, how Ophiocordyceps network attaches when it comes in contact with the host's muscle cells. Figure 15(c) illustrates how the fungus network is redistributing agent η, effect that is observable in the gradual coloration given by η red color marker.

6. Conclusions

We have presented a phase-field model for the simulation of fungal organisms that evolve in complex environments. Without loss of generality, the formulation focuses on developing the tools to capture the advanced phenomena exhibited by Ophiocordyceps network. This network operates in highly variable nutrient distributions (both in space and time), deals with constraints in the medium, and interacts with the surroundings through its geometrical features. The results indicate that our model can reproduce growth, migration, and decay processes observed in fungi. It is also sensitive to changes in nutrient distributions, fungal metabolic parameters, and boundary conditions. This sensitivity allows the model to reproduce a variety of colony global and local shapes that can actually be observed in nature. Moreover, we have explored the parameter space and provided a set of dimensionless numbers that control the pattern selection (i.e., pattern, branch thickness, and development). We have illustrated how these numbers can be used to simulate specific events, which showcase the capabilities of the model to reproduce time scales, overall mass structure amounts, and sudden changes in pattern behavior. The model is also successful in reproducing the mycelium growth in the presence of geometrical constraints, such as muscle cells in the Ophiocordyceps host, that may contain agents/nutrients able to be extracted and distributed within the network.

This work represents a first step in the pursue of a general framework able to capture the response of constrained interactive mycelia, such as Ophiocordyceps. Therefore, some simplifications have been applied. In particular, we have restricted most of the study to two-dimensional settings (we have demonstrated the capabilities of the model in three-dimensions, but have not performed a thorough analysis), and we have not incorporated an advective flow to the system. Likewise, we are aware that the parameters presented in this work can be linked or extended through more sophisticated metabolic descriptions, which would increase the model control and extend the range of patterns that can be reproduced (e.g., fractal-wise). Incorporating these elements remains a future line of work that should enable an in-depth analysis of Ophiocordyceps infectious process of Campotini ant's head, and other analogous pathogenic processes. Additionally, the energy variational framework on which the presented model is based turns it into a promising tool to explore the fundamental principles of network optimization displayed by fungi. Underpinning the physical principles and governing variables can be key in developing biologically inspired bottom-up strategies, applicable to fields such as medicine, transport networks, or swarm coordination.

7. Acknowledgments

Farshad Ghanbari and Christian Peco are grateful for the support of Penn State University. Computations for this research were performed on the Pennsylvania State University's Institute for Computational and Data Sciences Advanced CyberInfrastructure (ICDS-ACI). This research was supported in part by a Seed Grant award from the Institute for Computational and Data Sciences at the Pennsylvania State University. The authors gratefully acknowledge Patrick Hickey and Nemo Andrea for the experiment images used in the comparisons. Francesco Costanzo and David P. Hughes gratefully acknowledge the support of grant N. 5R01GM116927-05 the U.S. National Institutes of Health (NIGMS).

References

[1] Nick Couldry and Alison Powell. Big Data from the bottom up. *Big Data Soc.*, 2014.

[2] Kamaljit Singh, Bagus P Muljadi, Ali Q Raeini, Christian Jost, Veerle Vandeginste, Martin J Blunt, Guy Theraulaz, and Pierre Degond. The architectural design of smart ventilation and drainage systems in termite nests. *Sci. Adv.*, 5(3):eaat8520, 2019.

[3] Francesco Nazzi. The hexagonal shape of the honeycomb cells depends on the construction behavior of bees. *Sci. Rep.*, 6(1):28341, 2016.

[4] Atsushi Tero, Seiji Takagi, Tetsu Saigusa, Kentaro Ito, Daniel P Bebber, Mark D Fricker, Kenji Yumiki, Ryo Kobayashi, and Toshiyuki Nakagaki. Rules for biologically inspired adaptive network design. *Science*, 327(5964):439–442, 2010.

[5] Bruno Corrêa Barbosa, Vitor Ribeiro Halfeld, João Paulo Machado de Araújo, Tatiane Tagliatti Maciel, and Fábio Prezoto. Record of Ophiocordyceps unilateralis sensu lato, the zombie-ant fungus, parasitizing Camponotus in an urban fragment of Atlantic Rainforest in southeastern Brazil. *Stud. Neotrop. Fauna Environ.*, 50(1):21–23, 2015.

[6] David P Hughes, Sandra B Andersen, Nigel L Hywel-Jones, Winanda Himaman, Johan Billen, and Jacobus J Boomsma. Behavioral mechanisms and morphological symptoms of zombie ants dying from fungal infection. *BMC Ecol.*, 11(1):13, 2011.

[7] Sandra B Andersen, Sylvia Gerritsma, Kalsum M Yusah, David Mayntz, Nigel L Hywel-jones, Johan Billen, Jacobus J Boomsma, and David P Hughes. The Life of a Dead Ant : The Expression of an Adaptive Extended Phenotype. 174(3):424–433, 2009.

[8] Colleen A. Mangold, Melissa J. Ishler, Raquel G. Loreto, Missy L. Hazen, and David P. Hughes. Zombie ant death grip due to hypercontracted mandibular muscles. *J. Exp. Biol.*, 222(14):jeb200683, 2019.

[9] Maridel A Fredericksen, Yizhe Zhang, Missy L Hazen, Raquel G Loreto, Colleen A Mangold, Danny Z Chen, and David P Hughes. Three-dimensional visualization and a deep-learning model reveal complex fungal parasite networks in behaviorally manipulated ants. *Proc. Natl. Acad. Sci. U. S. A.*, 114(47):12590–12595, 2017.

[10] Fordyce A Davidson, Graeme P Boswell, Mark W F Fischer, Luke Heaton, Daniel Hofstadler, and Marcus Roper. Mathematical modelling of fungal growth and function. *IMA Fungus*, 2(1):33–37, 2011.

[11] J. H. Sietsma and J. G. H. Wessels. Apical wall biogenesis. Growth, Differentiation and Sexuality. In Ursula Kües and Reinhard Fischer, editors, *Mycota, A Compr. Treatise Fungi as Exp. Syst. Basic Appl. Res.*, pages 53–72. Springer Berlin-Heidelberg, 1994.

[12] Salomon Bartnicki-Garcia, David D Bartnicki, Gerhard Gierz, Rosamaría López-Franco, and Charles E Bracker. Evidence That Spitzenkörper Behavior Determines the Shape of a Fungal Hypha: A Test of the Hyphoid Model. *Exp. Mycol.*, 19(2):153–159, 1995.

[13] Salomon Bartnicki-garcia, Charles E Bracker, and Gerhard Gierz. Mapping the Growth of Fungal Hyphae : Orthogonal Cell Wall Expansion during Tip Growth and the Role of Turgor. 79:2382–2390, 2000.

[14] C M Regalado, B D Sleeman, and K Ritz. Aggregation and collapse of fungal wall vesicles in hyphal tips: a model for the origin of the Spitzenkörper. *Philos. Trans. R. Soc. Lond. B. Biol. Sci.*, 352(1364):1963–1974, 1997.

[15] Simon H. Tindemans, Norbert Kern, and Bela M. Mulder. The diffusive vesicle supply center model for tip growth in fungal hyphae. *J. Theor. Biol.*, 238(4):937–948, 2006.

[16] F. Soddell, R. Seviour, and J. Soddell. Using Lindenmayer systems to investigate how filamentous fungi may produce round colonies. *Complex. Int.*, 2(ISSN 1320), 1995.

[17] C.M. Regalado, J.W. Crawford, K. Ritz, and B.D. Sleeman. The origins of spatial heterogeneity in vegetative mycelia: a reaction-diffusion model. *Mycol. Res.*, 100(12):1473–1480, 1996.

[18] Audrius Meskauskas, Liam J McNulty, and David Moore. Concerted regulation of all hyphal tips generates fungal fruit body structures: experiments with computer visualizations produced by a new mathematical model of hyphal growth. *Mycol. Res.*, 108(Pt 4):341–353, 2004.

[19] Audrius Meskauskas, Mark D Fricker, and David Moore. Simulating colonial growth of fungi with the Neighbour-Sensing model of hyphal growth. *Mycol. Res.*, 108(Pt 11):1241–1256, 2004.

[20] J. I. Prosser and A. P. J. Trinci. A Model for Hyphal Growth and Branching. *J. Gen. Microbiol.*, 111(1):153–164, 1979.

[21] H Yang, R King, U Reichl, and E D Gilles. Mathematical model for apical growth, septation, and branching of mycelial microorganisms. *Biotechnol. Bioeng.*, 39(1):49–58, 1992.

[22] F. López-Isunza, C.P. Larralde-Corona, and G. Viniegra-González. Mass transfer and growth kinetics in filamentous fungi. *Chem. Eng. Sci.*, 52(15):2629–2639, 1997.

[23] Wellington Balmant, Maura Harumi Sugai-Guérios, Juliana Hey Coradin, Nadia Krieger, Agenor Furigo, and David Alexander Mitchell. A model for growth of a single fungal hypha based on well-mixed tanks in series: Simulation of nutrient and vesicle transport in aerial reproductive hyphae. *PLoS One*, 10(3), 2015.

[24] Graeme P Boswell, Helen Jacobs, Karl Ritz, Geoffrey M Gadd, Fordyce A Davidson, and Et al. The development of fungal networks in complex environments. *Bull. Math. Biol.*, 69(2):605–634, feb 2007.

[25] C A Gilligan and D J Bailey. Components of pathozone behaviour. *New Phytol.*, 136(2):343–358, 1997.

[26] L. Edelstein and L.A. Segel. Growth and metabolism in mycelial fungi. *J. Theor. Biol.*, 104(2):187–210, 1983.

[27] Leah Edelstein-Keshet and Bard Ermentrout. Models for Branching Networks in Two Dimensions. *SIAM J. Appl. Math.*, 49(4):1136–1157, 1989.

[28] F.A. Davidson, B.D. Sleeman, A.D.M. Rayner, J.W. Crawford, and K. Ritz. Large-Scale Behavior of Fungal Mycelia. 24(10):81–87, 1996.

[29] F A Davidson. A Mathematical Model for Fungal Development in Heterogeneous Environments asex. 11(6):51–56, 1998.

[30] A J Stacey, J E Truscott, C A Gilligan, A J Stacey, J E Truscott, and C A Gilligan. Soil-Borne Fungal Pathogens : Scaling-Up from Hyphal to Colony Behaviour and the Probability of Disease Transmission. *New Phytol.*, 150(1):169–177, 2001.

[31] Juan M. López and Henrik J. Jensen. Generic model of morphological changes in growing colonies of fungi ´. *Phys. Rev. E*, 65:1–5, 2002.

[32] Graeme P Boswell, Helen Jacobs, Fordyce A Davidson, Geoffrey M Gadd, and Karl Ritz. Functional Consequences of Nutrient Translocation in Mycelial Fungi. *J. Theor. Biol.*, 217(4):459–477, 2002.

[33] Graeme P Boswell, Helen Jacobs, Geoffrey M Gadd, Karl Ritz, and Fordyce A Davidson. A mathematical approach to studying fungal mycelia. *Mycologist*, 17(November):165–171, 2003.

[34] Graeme P Boswell, Helen Jacobs, Fordyce A Davidson, Geoffrey M Gadd, and Karl Ritz. Growth and function of fungal mycelia in heterogeneous environments. *Bull. Math. Biol.*, 65:447–477, 2003.

[35] Ruth E Falconer, James L Bown, Nia A White, and John W Crawford. Biomass recycling and the origin of phenotype in fungal mycelia. *Proc. R. Soc. B*, 272:1727–1734, 2005.

[36] E Z Panagou, P N Skandamis, and G.-J.E. Nychas. Modelling the combined effect of temperature, pH and aw on the growth rate of Monascus ruber, a heat-resistant fungus isolated from green table olives. *J. Appl. Microbiol.*, 94(1):146–156, 2003.

[37] J S Rowlinson. Translation of J. D. van der Waals' "The thermodynamik theory of capillarity under the hypothesis of a continuous variation of density". *J. Stat. Phys.*, 20(2):197–200, 1979.

[38] J W Cahn and J E Hillard. Free energy of a nonuniform system. I. Interfacial free energy. *J. Chem. Phys.*, 28:258, 1958.

[39] B. Li, C. Peco, D. Millán, I. Arias, and M. Arroyo. Phase-field modeling and simulation of fracture in brittle materials with strongly anisotropic surface energy. *Int. J. Numer. Methods Eng.*, 102(3-4):711–727, 2015.

[40] B. W. Spencer, W. Jiang, J. E. Dolbow, and C. Peco. Pellet cladding mechanical interaction modeling using the extended finite element method. *Top Fuel 2016 LWR Fuels with Enhanc. Saf. Perform.*, pages 929–938, 2016.

[41] C. Peco, W. Chen, Y. Liu, M. M. Bandi, J. E. Dolbow, and E. Fried. Influence of surface tension in the surfactant-driven fracture of closely-packed particulate monolayers. *Soft Matter*, 13(35):5832–5841, 2017.

[42] A. Rosolen, C. Peco, and M. Arroyo. An adaptive meshfree method for phase-field models of biomembranes. Part I: Approximation with maximum-entropy basis functions. *J. Comput. Phys.*, 249, 2013.

[43] C. Peco, A. Rosolen, and M. Arroyo. An adaptive meshfree method for phase-field models of biomembranes. Part II: A Lagrangian approach for membranes in viscous fluids. *J. Comput. Phys.*, 249:320–336, 2013.

[44] Rui D M Travasso, Eugenia Corvera Poiré, Mario Castro, Juan Carlos Rodríguez-manzaneque, and A Hernández-Machado. Tumor Angiogenesis and Vascular Patterning : A Mathematical Model. *PLoS One*, 6(5):e19989, 2011.

[45] Guillermo Vilanova, Ignasi Colominas, and Hector Gomez. Capillary networks in tumor angiogenesis: From discrete endothelial cells to phase-field averaged descriptions via isogeometric analysis. *Int. j. numer. method. biomed. eng.*, 29(10):1015–1037, 2013.

[46] Jiangping Xu, Guillermo Vilanova, and Hector Gomez. A Mathematical Model Coupling Tumor Growth and Angiogenesis. *PLoS One*, 11(2):1–20, 2016.

[47] Guillermo Vilanova, Ignasi Colominas, and Hector Gomez. A mathematical model of tumour angiogenesis : growth , regression and regrowth. *J. R. Soc. Interface*, 14, 2017.

[48] Guillermo Vilanova, Ignasi Colominas, and Hector Gomez. Computational Modeling of Tumor-Induced Angiogenesis. *Arch. Comput. Methods Eng.*, 24(4):1071–1102, 2017.

[49] Jiangping Xu, Guillermo Vilanova, and Hector Gomez. ScienceDirect Phase-field model of vascular tumor growth : Three-dimensional geometry of the vascular network and integration with imaging data. *Comput. Methods Appl. Mech. Eng.*, 359:112648, 2020.

[50] Ernesto A B F Lima, Regina C Almeida, and J Tinsley Oden. Analysis and numerical solution of stochastic phase-field models of tumor growth. *Numer. Methods Partial Differ. Equ.*, 31(2):552–574, 2015.

[51] Shiva Rudraraju, Anton Van der Ven, and Krishna Garikipati. Mechanochemical spinodal decomposition: a phenomenological theory of phase transformations in multi-component, crystalline solids. *npj Comput. Mater.*, 2(1):16012, 2016.

[52] C. Peco, D. Millán, A. Rosolen, and M. Arroyo. Efficient implementation of Galerkin mesh-free methods for large-scale problems with an emphasis on maximum entropy approximants. *Comput. Struct.*, 150:52–62, 2015.

[53] Derek Gaston, Chris Newman, Glen Hansen, and Damien Lebrun-Grandié. MOOSE: A parallel computational framework for coupled systems of nonlinear equations. *Nucl. Eng. Des.*, 239(10):1768–1778, 2009.

[54] C. Peco, Y. Liu, C. Rhea, and J. E. Dolbow. Models and simulations of surfactant-driven fracture in particle rafts. *Int. J. Solids Struct.*, 156-157:194–209, 2019.

[55] D. H. Bergey and Eds. Holt, John G. *Bergey's Manual Of Determinative Bacteriology.* 2000.

[56] Patrick Hickey. Fungi time-lapse https://www.youtube.com/watch?v=i9T727tz7FA Mould, mycelium and bioluminescence, 2014.

[57] Nemo Andrea. Oat Hunt (4K) https://youtu.be/99POSqAOra8 Physarum Polycephalum , 2018.